Geochemistry Geophysics Geosystems G3

Article
Volume 13, Number 1
20 January 2012
Q01014, doi:10.1029/2011GC003892
ISSN: 1525-2027

Published by AGU and the Geochemical Society

Magma chamber properties from integrated seismic tomography and thermal modeling at Montserrat

M. Paulatto
Department of Earth Sciences, University of Oxford, South Parks Road, Oxford OX1 3AN, UK (michelep@earth.ox.ac.uk)

National Oceanography Centre, Southampton, University of Southampton, European Way, Southampton SO14 3ZH, UK

C. Annen
Department of Earth Sciences, University of Bristol, Wills Memorial Building, Queen's Road, Bristol BS8 1RJ, UK

T. J. Henstock
National Oceanography Centre, Southampton, University of Southampton, European Way, Southampton SO14 3ZH, UK

E. Kiddle
Department of Earth Sciences, University of Bristol, Wills Memorial Building, Queen's Road, Bristol BS8 1RJ, UK

T. A. Minshull
National Oceanography Centre, Southampton, University of Southampton, European Way, Southampton SO14 3ZH, UK

R. S. J. Sparks
Department of Earth Sciences, University of Bristol, Wills Memorial Building, Queen's Road, Bristol BS8 1RJ, UK

B. Voight
Department of Geosciences, Pennsylvania State University, University Park, Pennsylvania 16802, USA

[1] It is widely believed that andesitic magmas erupted at arc-volcanoes are stored in shallow reservoirs prior to eruption, but high-resolution images of focused regions of magma in the shallow crust are rare. We integrate seismic tomography with numerical models of magma chamber growth to constrain the magma chamber beneath Soufrière Hills Volcano, Montserrat. Our approach reveals the characteristics and dynamics of the magmatic system with a level of detail that no single method has yet achieved. The integrated analysis suggests that a magma chamber of 13 km^3 with over 30% melt fraction formed between 5.5 and at least 7.5 km depth, a significantly higher melt fraction than inferred from the seismic data alone. The magma chamber may have formed by incremental sill intrusion over a few thousand years and is likely to be a transient, geologically short-lived feature. These volume and geometry estimates are critical parameters to model eruption dynamics, which in turn are key to hazard assessment and eruption forecasting.

Components: 8700 words, 13 figures.

Keywords: arc volcano; magma chamber; seismic tomography; thermal modeling.

Index Terms: 7270 Seismology: Tomography (6982, 8180); 8185 Tectonophysics: Volcanic arcs; 8439 Volcanology: Physics and chemistry of magma bodies.

Received 23 September 2011; **Revised** 2 December 2011; **Accepted** 12 December 2011; **Published** 20 January 2012.

Paulatto, M., C. Annen, T. J. Henstock, E. Kiddle, T. A. Minshull, R. S. J. Sparks, and B. Voight (2012), Magma chamber properties from integrated seismic tomography and thermal modeling at Montserrat, *Geochem. Geophys. Geosyst.*, *13*, Q01014, doi:10.1029/2011GC003892.

1. Introduction

[2] Modeling of magmatic system dynamics requires accurate estimates of magma chamber geometry and properties, but attempts to constrain these characteristics with seismic and other techniques have produced mixed and sometimes conflicting results [*Lees*, 2007; *Voight et al.*, 2010a]. Uncertainty in the rheological properties of the crust and insensitivity of ground deformation to source shape make it hard to uniquely constrain magma storage regions with geodetic techniques [*Voight et al.*, 2010a; *Mattioli et al.*, 2010; *Foroozan et al.*, 2010]. Broad low-seismic-velocity regions, often interpreted as evidence of melt, have been identified with both active and passive seismic tomography techniques beneath many active volcanoes, but high-resolution images of focused magma storage regions are rare [*Lees*, 2007; *Brandsdottir et al.*, 1997; *Alfaro et al.*, 2007]. No such images exist for andesite volcanoes, since active seismic experiments at island arcs have lacked the resolution to image the details of upper-crustal magmatic systems [*Christeson et al.*, 2008]. Despite these difficulties, active seismic surveys are well suited to image volcanoes in oceanic settings, where a large number of artificial seismic signals can be generated by towed airguns, and arrays of land and seafloor seismometers can record these signals and provide high-resolution images of the subsurface even in the presence of complex three-dimensional structures [*Seher et al.*, 2010; *Evangelidis et al.*, 2004]. Using this approach we present here a new three-dimensional seismic velocity model of the upper crust at Montserrat, Lesser Antilles, from active-source wide-angle seismic data [*Voight et al.*, 2010b].

[3] The island of Montserrat, in the Lesser Antilles, is an ideal target for a seismic tomography experiment, because of its small size, relatively simple volcanic history, and the need to better understand the 1995 eruption. Montserrat is composed of the lava domes and associated pyroclastic deposits of three andesite volcanoes, Silver Hills (SH, 2600–1200 ka), Centre Hills (CH, 950–550 ka) and the Soufrière Hills Volcano (SHV, 170 ka–present) (Figure 1). The three volcanoes have very similar petrology and a clear age progression from north to south [*Harford et al.*, 2002], making it possible to study them comparatively. Volcanic activity started in 1995 after over three centuries of quiescence and was preceded by a series of periods of increased seismic activity [*Shepherd et al.*, 1971; *Aspinall et al.*, 1998]. The activity is characterized by the growth of an andesite lava dome and associated dome collapses, explosions and pyroclastic flows. The eruption is still ongoing in 2011 and has so far consisted of five eruptive phases of continuous lava extrusion interrupted by periods of quiescence.

[4] The magmatic system of SHV is thought to be composed of four main elements: a primary source of mafic magma in the mantle wedge [*Zellmer et al.*, 2003], a mid-crustal magma storage region where andesite is generated by fractionation of basalt [*Elsworth et al.*, 2008], a shallow magma reservoir, where andesite resides prior to eruption and undergoes further transformation [*Murphy et al.*, 2000], and a strato-volcano, consisting of a core of lava domes and a soft apron of volcaniclastic deposits [*Harford et al.*, 2002; *Paulatto et al.*, 2010a; *Shalev et al.*, 2010]. Some characteristics of the shallow magma reservoir have been constrained with petrological and geodetic data. Analysis of SHV andesites and modeling of ground deformation and magma efflux suggest that the shallow magma chamber lies at approximately 5–7 km depth, but details on its geometry are debated [*Murphy et al.*, 2000; *Voight et al.*, 2006; *Elsworth et al.*, 2008; *Voight et al.*, 2010a; *Mattioli et al.*, 2010; *Foroozan et al.*, 2010]. Pyroxene geothermometry indicates that the magma is relatively cool (~850°C) and highly crystalline (60–65 vol%) [*Murphy et al.*, 2000]. Tomographic studies imaged the subsurface at

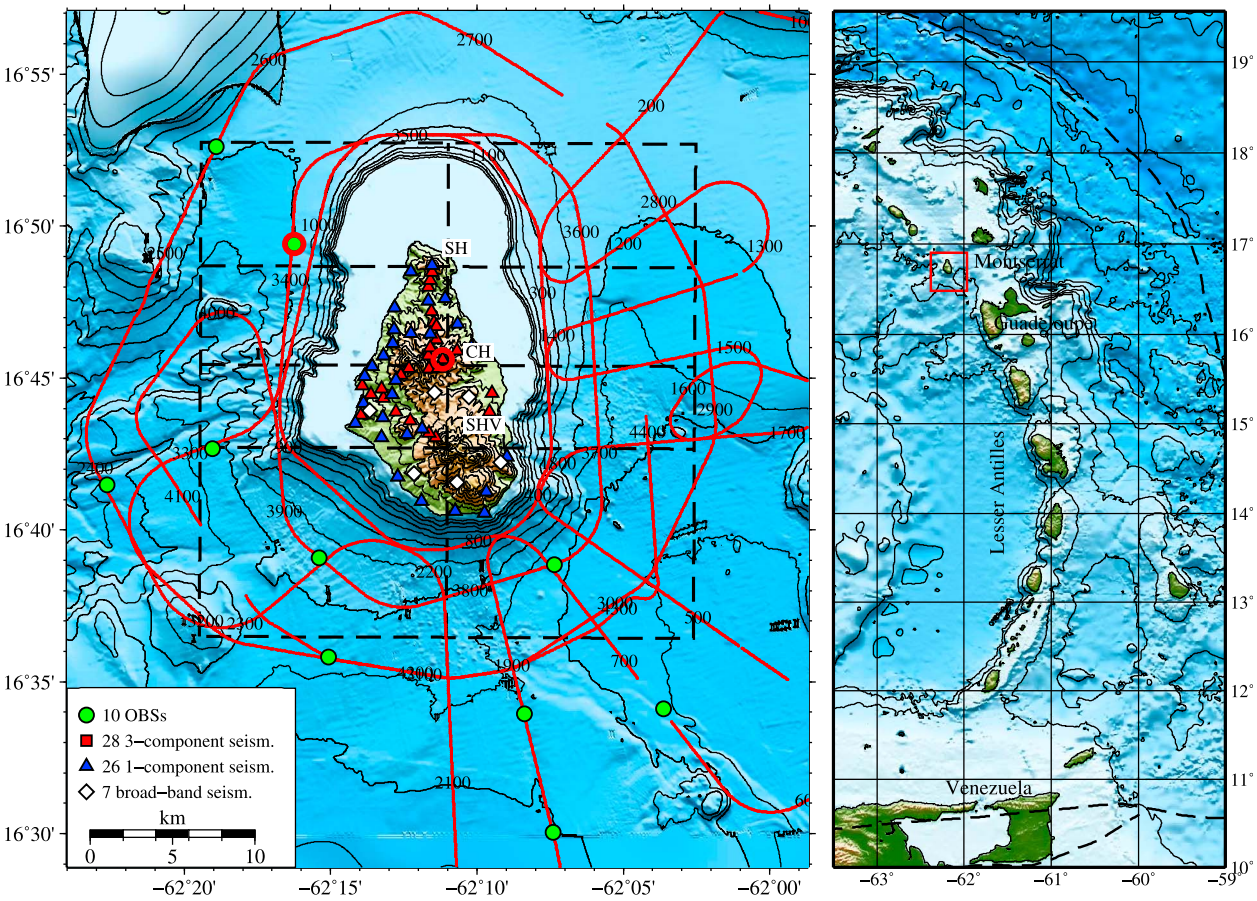

Figure 1. Topographic map of survey area with recording array and shot positions. Contour interval is 200 m. A total of 4414 shots were fired at approximately 140 m spacing (red line). Shot numbers are labeled every 100 shots. The locations of the sections shown in Figure 9 are marked with black dashed lines. The stations corresponding to the data shown in Figures 2 and 3 are highlighted in red. (right) The location of Montserrat in the Lesser Antilles. Plate boundaries from *Coffin et al.* [1998]. Digital elevation model from *Le Friant et al.* [2004] and the GEBCO_08 Grid (http://www.gebco.net).

Montserrat [*Paulatto et al.*, 2010a; *Shalev et al.*, 2010], but have lacked the resolution beyond 5 km depth to constrain the shallow crustal magma chamber. We present an improved three-dimensional seismic velocity model obtained by regularized inversion of first arrival travel-times [*Hobro et al.*, 2003] from additional active-source wide-angle seismic data recorded on an array of land and ocean-bottom seismometers (OBSs).

2. Experiment and Data

[5] The data set analyzed in this study was collected in December 2007 as part of the SEA-CALIPSO project [*Voight et al.*, 2010b]. The tomographic inversion is based on 181,665 first arrival traveltimes from 4414 airgun shots recorded on a land-sea seismic station array (Figure 1). The array consisted of 10 ocean bottom seismometers, provided by the UK Ocean Bottom Instrumentation Consortium [*Minshull et al.*, 2005] and 244 land seismometers including 28 three-component short-period seismometers and 209 vertical geophones, provided by the Incorporated Research Institutions for Seismology, and 7 broad-band seismometers of the Montserrat Volcano Observatory permanent seismic network. The OBSs were equipped with a hydrophone and a one- or three-component seismometer. To pick travel-times we mostly used the hydrophone channels since they were generally of higher quality. The vertical components of 61 land stations were used in this study, selected to provide a regular coverage of the island. The seismic source was a 2600 cu. in. (42.61 l) airgun array consisting of eight Sercel G-guns fired at 2000 psi (1.382×10^7 Pa) and towed behind the RRS James Cook at 10 m depth. The firing interval was 60 s and the average speed was 4.5 knots (2.3 m s^{-1}), giving an

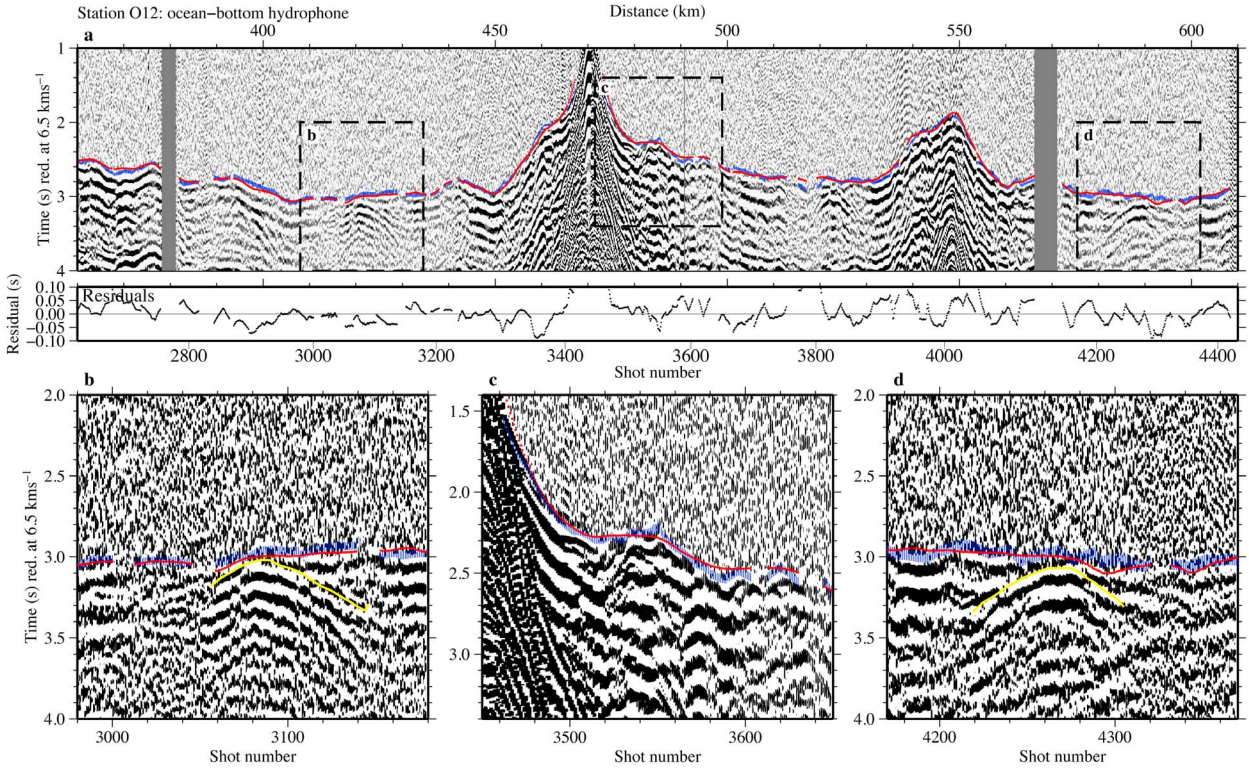

Figure 2. Example OBS data. (a) Receiver gather for an OBS hydrophone channel. Picked first arrival travel-times with error bars are marked in blue. Synthetic travel-times for the final model are marked in red. The distance along the ship track from the start of shooting is marked above the section and shot numbers are marked below. For location see Figure 1. The panel below the data section shows travel-time residuals. (b–d) Detailed panels showing data fit. Examples of secondary phases are marked in yellow.

average shot spacing of 139 m. Shooting was performed continuously over a series of radial lines and circles around the island of Montserrat (Figure 1). Coincident multichannel reflection data were also collected during the survey [*Kenedi et al.*, 2010].

[6] Example receiver gathers for a hydrophone channel on an ocean-bottom instrument and a land seismometer vertical component are shown in Figures 2 and 3 respectively. First arrivals can be identified at up to 50 km offset and were picked for 10–92% of the shot recordings depending on noise levels. Pick uncertainties were estimated visually and first assigned depending on source-receiver offset: 30 ms for offset <10 km, 40 ms for 10 km < offset <20 km, 50 ms for 20 km < offset <30 km, 60 ms for 30 km < offset <40 km, 70 ms for offset >50 km. Uncertainties were then corrected by a factor of 1.0, 1.5 or 2.0 based on general noise levels of the stations. Wide-angle reflections were also observed and were used in the preliminary 2d inversion of a subset of the data [*Paulatto et al.*, 2010a]. Only first arrivals were used in the 3d inversion as it was not possible to identify a consistent reflection from acoustic basement or any other interface in the wide-angle and zero-offset data over the whole survey area. Examples of observed secondary phases are marked in Figures 2b and 2d. The absence of a clear and consistent acoustic basement is likely due to the complex and long history of the Lesser Antilles arc.

[7] Horizontal components were available for some instruments, including 7 three-component OBSs, 28 short-period seismometers and 7 broad-band seismometers. Converted shear waves can provide a more robust characterization of fluid content, but were not used in this study as we could not identify and pick them confidently. Identification is difficult because of the complex shooting geometry and the low signal-to-noise ratios for raypaths crossing SHV. In addition there's no abrupt impedance contrast at top of basement, so it may be that mode conversions are weak or absent.

[8] Some characteristics of the upper crustal structure can be inferred directly from the raw data. Field recordings at OBS stations show delayed first arrivals and decreased signal-to-noise ratio for

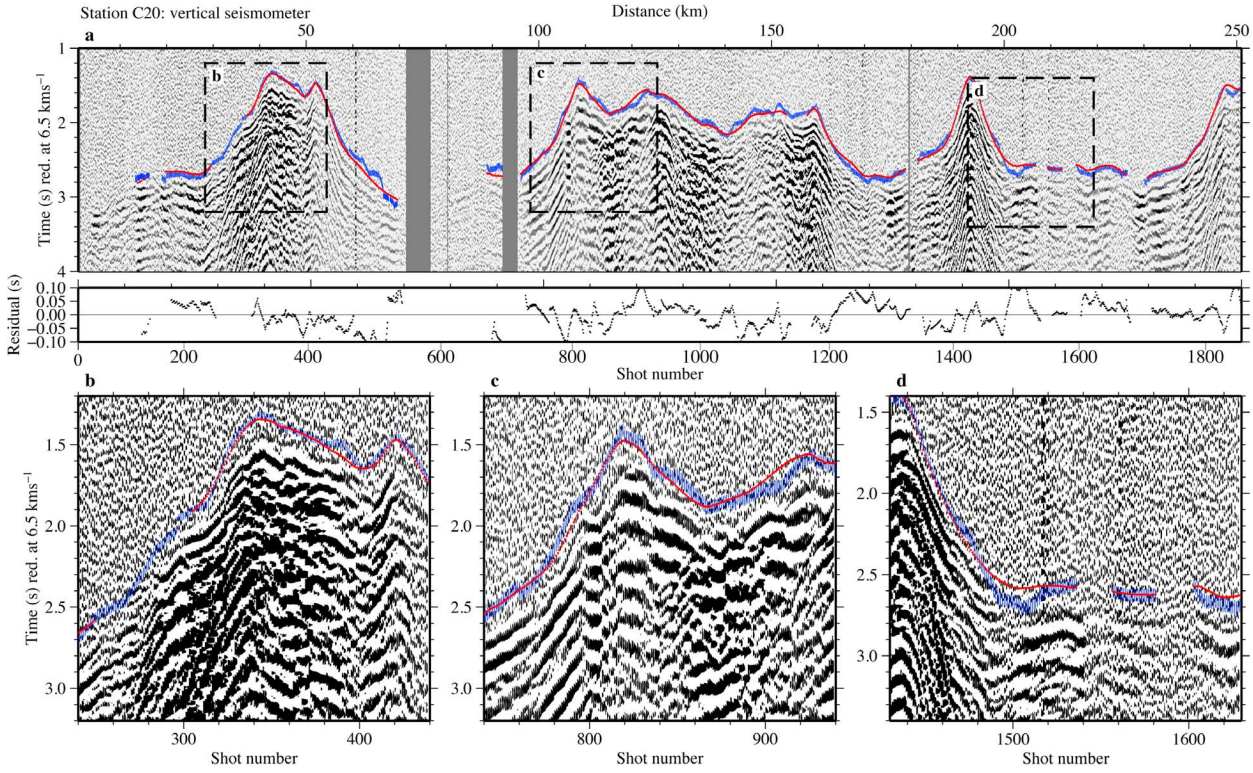

Figure 3. Example land data. (a) Receiver gather for a vertical land seismometer. Picked first arrival travel-times with error bars are marked in blue. Synthetic travel-times for the final model are marked in red. The distance along the ship track from the start of shooting is marked above the section and shot numbers are marked below. For location see Figure 1. The panel below the data section shows travel-time residuals. (b–d) Detailed panels showing data fit.

seismic waves undershooting SHV (Figure 4), a signature often associated with the presence of magma bodies. The delay is matched closely by synthetic first arrivals for the final model but not by first arrivals from an earlier smoother model (Figure 5, iteration 36), suggesting that the source of the delay is captured in our final model. The delay is larger for offsets of 30–40 km, corresponding to rays turning at 6–7 km depth, and has a maximum of about 0.2 s. The reduced signal-to-noise ratio is likely due to the shadow zone of a low-seismic velocity body and to enhanced attenuation caused by strong scattering by geological heterogeneities corresponding to solidified intrusions and/or by the presence of partial melt beneath SHV [*Paulatto et al.*, 2010b].

3. Three-Dimensional Seismic Velocity Model

3.1. Seismic Tomography Method

[9] We inverted first arrival traveltimes to generate a three-dimensional seismic velocity model using a tomography code based on the regularized least squares approach [*Hobro et al.*, 2003]. The algorithm allows a realistic multilayer model parameterization. Seismic velocities are defined by interpolating a quadratic b-spline polynomial over a regular rectangular grid. The grid spacing was set to 1 km in all directions in the early inversion iterations. The vertical grid spacing was reduced to 0.5 km after iteration 36 (Figure 5) to allow stronger vertical velocity gradients. The model is continuous and smooth within each layer, but it can be discontinuous across interfaces separating different layers. Interfaces are defined by interpolation of a cubic b-spline polynomial over a regular 200 m grid. The starting model (Figure 5) was composed of three laterally homogeneous layers, separated by interfaces representing the seabed and sea surface. The top or first layer is an air layer with constant v_P = 0.34 km s^{-1}. The second layer is a water layer with v_P decreasing from 1.53 km s^{-1} at the surface to 1.49 km s^{-1} at 1 km depth. The third layer is a solid layer with initial laterally homogeneous velocity structure determined from a two-dimensional inversion of a subset of the data [*Paulatto et al.*, 2010a].

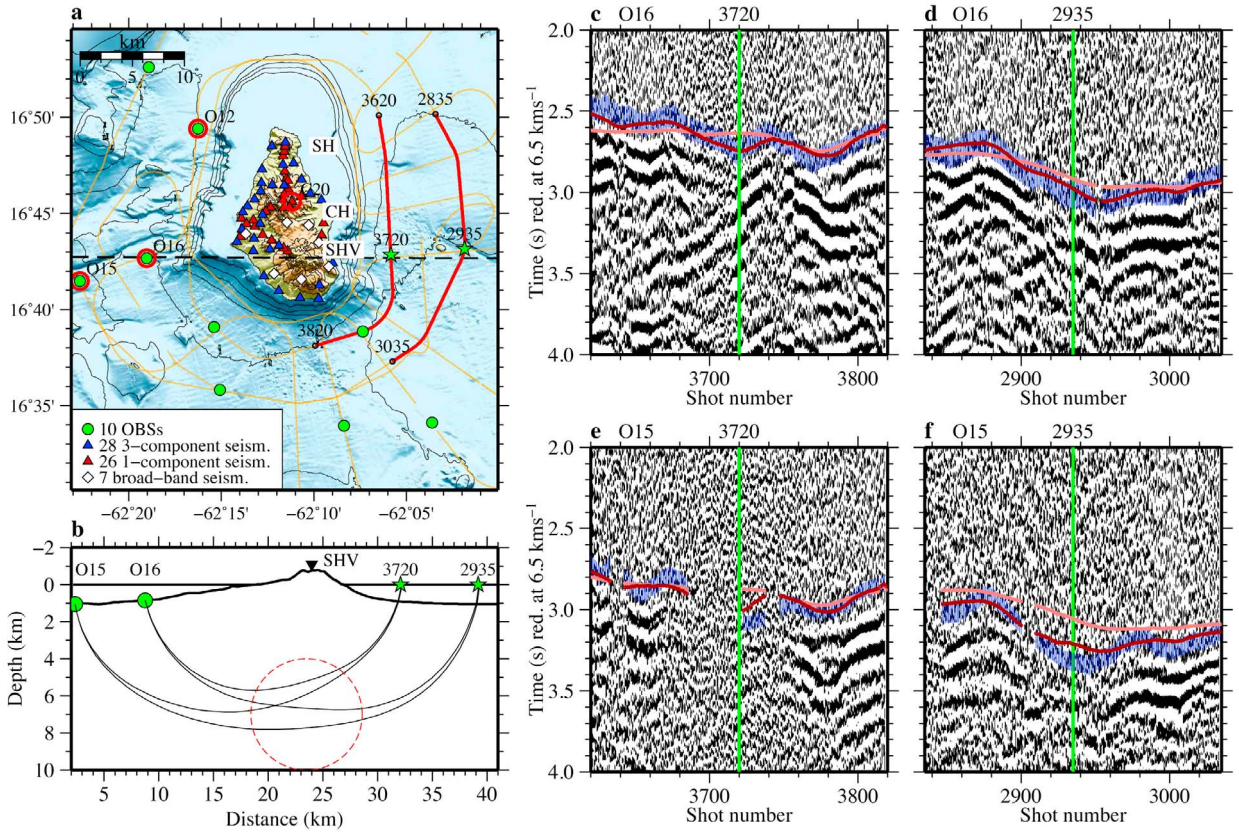

Figure 4. Field recordings showing delayed first arrivals and reduced signal-to-noise ratio beneath SHV. (a) Map with location of instruments and data sections. Ship track in orange, shots corresponding to sections shown in Figures 4b–4f are highlighted in red. (b) Section through SHV, corresponding to dashed line in a, showing topography and ray trajectories. The approximate extent of the low velocity volume is marked with a dashed red line. (c–f) Data corresponding to shots highlighted in Figure 4a. First arrivals with error bars in blue. Travel-times for final model in red. Travel-times for smooth model in pink (Figure 5, iteration 36). The traces highlighted in green correspond to shots highlighted with stars in Figure 4a.

[10] The best fitting model was estimated by iteratively minimizing a linearized-least squares functional of the form

$$\Psi(\delta\mathbf{m}) = \delta\mathbf{t}_l^T \mathsf{C}_D^{-1} \delta\mathbf{t}_l + \lambda_m (\mathbf{m}_0 + \delta\mathbf{m})^T \mathsf{C}_M^{-1} (\mathbf{m}_0 + \delta\mathbf{m}) \quad (1)$$

where $\delta\mathbf{m}$ is the model update vector, $\mathbf{m}_0$ is the previous model and $\delta\mathbf{t}_l = \mathbf{r} - \mathsf{A}\delta\mathbf{m}$ is the misfit vector, with $\mathbf{r}$ the travel-time residuals and A the matrix of Fréchet derivatives. Synthetic travel-times and Fréchet derivatives were calculated with a ray shooting approach [*Virieux and Farra*, 1991]. The functional is designed to reduce the data residuals while keeping the model roughness low, to avoid introducing features that are not required by the data. The first term of the functional represents the misfit, i.e. the quadratic difference between recorded and synthetic travel-times. The travel-time misfits are weighted by the elements of the diagonal data covariance C_D which are proportional to the reciprocals of the squares of the pick uncertainties. The second term is a smoothing operator governed by the model covariance matrix C_M and its relative magnitude can be varied by changing the regularization constant λ_m. In this case C_M is defined by a Laplace operator [*Hobro et al.*, 2003].

3.2. Inversion in Practice

[11] The inversion process consists of iteratively modifying the starting model to gradually reduce the objective function. At the beginning of the inversion the regularization constant is kept high to derive a smooth average model, ensuring that the subsequent steps do not depend on the starting model and reducing the operator bias. Then the smoothing is gradually reduced and more detailed structure is allowed to appear in the model (Figure 5). After iteration 48 the average residual of each station was adopted as station correction to

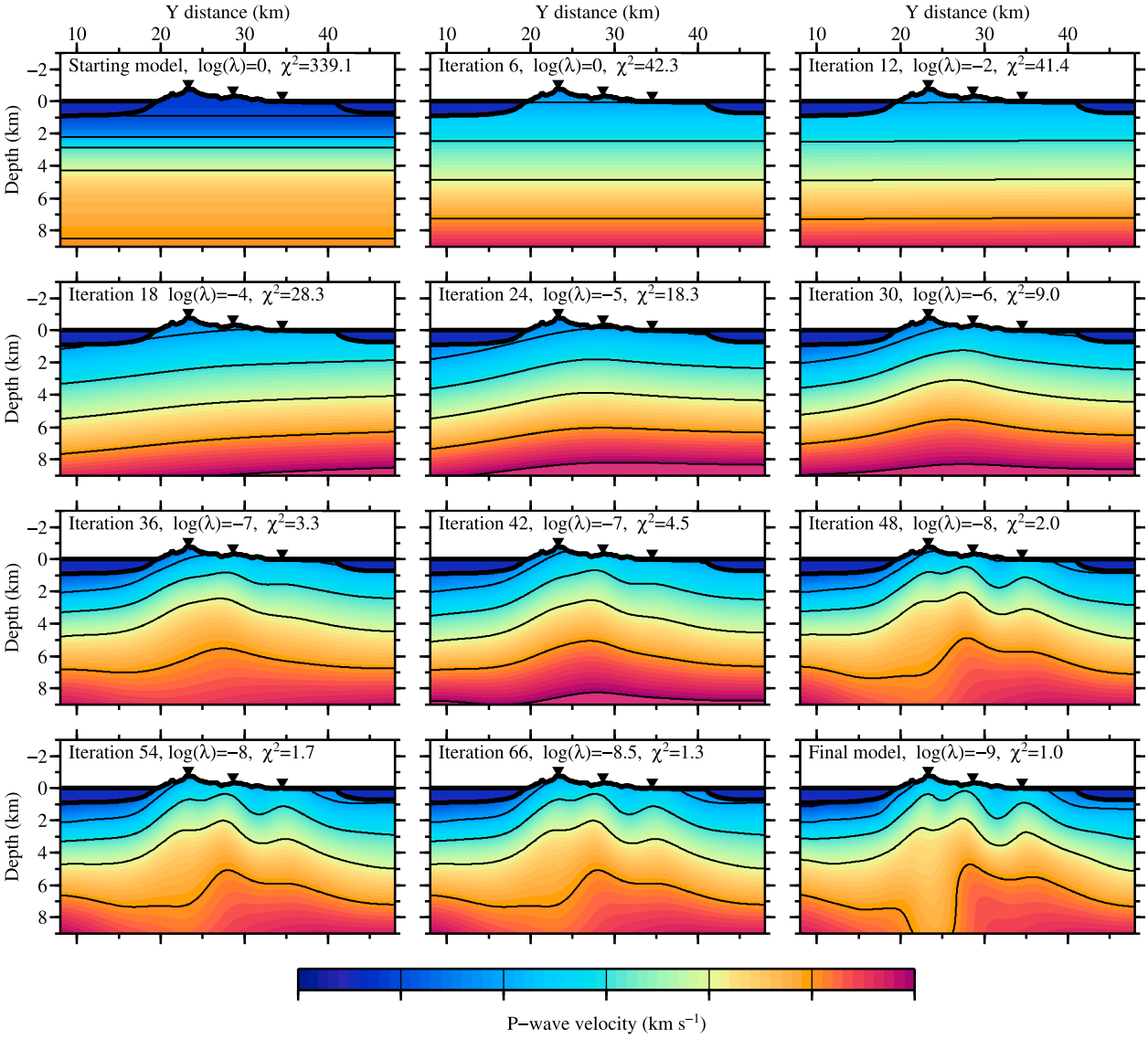

Figure 5. S-N sections along DD′ through the model at different stages of the inversion, from starting to final model.

account for shallow variations that have spatial dimensions smaller than the grid spacing. The inversion was halted when the residuals were on average of the same magnitude as the travel-time uncertainties (normalized chi squared = 1). The root mean square (RMS) residual was reduced from 891 ms in the starting model to 55 ms in the final model. The initial RMS residual and initial chi squared are very large because the starting model was built based on OBS data alone and is therefore representative of the offshore structure but not of the island structure. Average station residuals for the starting model are low for all OBS stations and large and negative for most land stations (Figure 6), suggesting that the seismic velocity beneath the island is faster than in the surroundings, as already observed in previous studies [*Paulatto et al.*, 2010a; *Shalev et al.*, 2010] and confirmed by our velocity model.

3.3. Model Resolution

[12] A first estimate of the model resolution was obtained by calculating the ray density in each model cell. The deepest rays turn at about 12 km depth and the shallowest at a few hundred meters beneath the seabed (Figure 7). The ray coverage is densest at about 3 km depth beneath the island and decreases beneath 5 km depth where most land-station rays reach their deepest point. Beneath this depth the model is constrained predominantly by

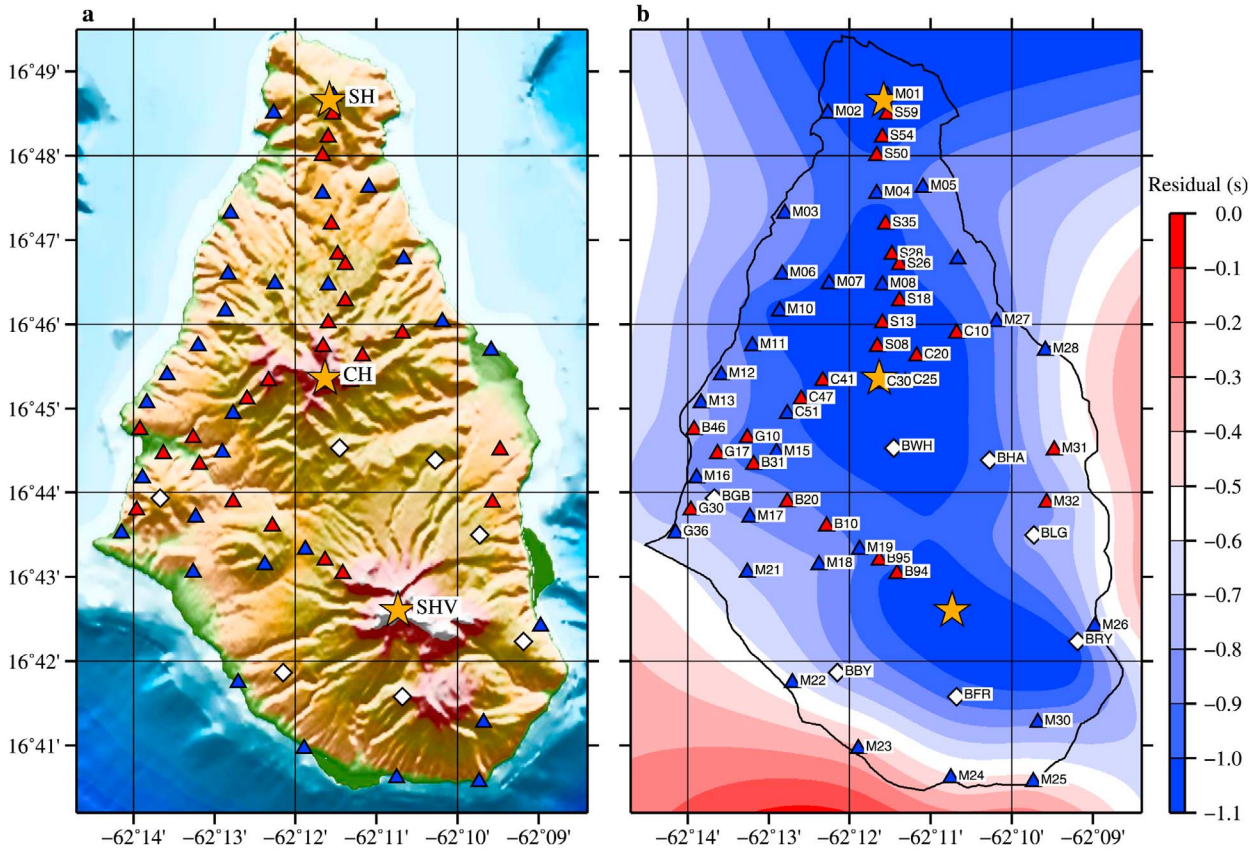

Figure 6. (a) Topographic map of the island with land array. (b) Color map of average station residuals of starting model. Station symbols as in Figure 1. Orange stars mark the summits of the three volcanic centers.

rays undershooting the island, recorded at seafloor instruments.

[13] Checkerboard tests [*Zelt*, 1998] were carried out with patterns of varying lateral and vertical dimension. Each test consisted of inverting a synthetic data set obtained by ray tracing in a perturbed model built by superimposing an 8% three-dimensional sinusoidal seismic velocity perturbation to the final model. Random Gaussian errors with variance equal to the original pick uncertainties were added to the synthetic travel-times to simulate the effect of noise in the recordings. In regions where the difference between the initial and recovered perturbation is small the model is well resolved. The similarity between the initial and recovered perturbation was assessed by calculating the semblance with a spherical convolution operator [*Zelt*, 1998; *Seher et al.*, 2010]. For each cell size the calculation was repeated with checkerboard pattern shifted by a half of a cell size in each direction, giving a series of eight different patterns for each cell size, to avoid biasing the result with a particular choice of pattern alignment. The mean semblance for each cell size is plotted in Figure 8 next to an example recovered perturbation. In areas of the model with semblance above 0.7 the pattern is generally thought to be well constrained [*Zelt*, 1998; *Seher et al.*, 2010] and our results confirm this convention. The low-velocity volume (LVV) is about the size of a cell of pattern C (Figure 8e), therefore it is well constrained to a depth of up to 7.5 km.

[14] The seismic resolution length was estimated throughout the model by interpolation and is given by the cell size that would yield a semblance of 0.7. The resolution is limited in the top 2 km by the irregular sampling and by the fact that most rays are sub-parallel and is best between 2 and 6 km where the ray coverage is higher and rays cover a large range of azimuths. Between 6 and 7.5 km the resolution is still acceptable, but decreases gradually and then drops quickly beneath 7.5 km depth.

4. Results

4.1. Seismic Velocity Structure

[15] The final seismic velocity model shows that the three volcanic centers share a similar shallow

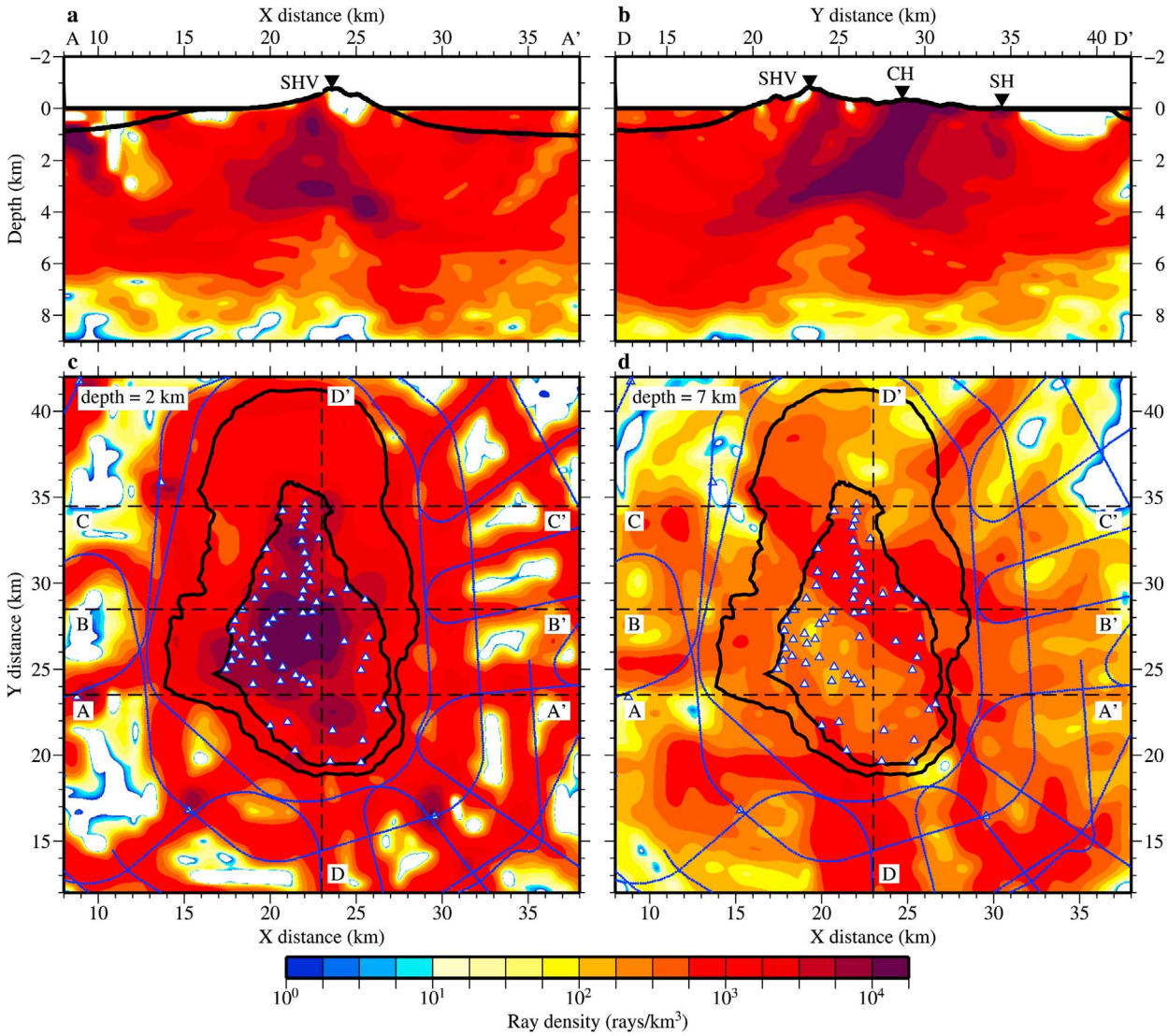

Figure 7. Ray density. (a) W-E section. (b) S-N section. (c, d) Horizontal sections at 2 and 7 km depth respectively.

structure, characterized by a prominent high-seismic-velocity core, likely comprising lava domes and intrusions, surrounded by a lower-seismic-velocity apron of volcaniclastic and pelagic sediments, in agreement with previous tomographic models [*Paulatto et al.*, 2010a; *Shalev et al.*, 2010] (Figure 9). At depths larger than 4 km, the three volcanoes are strikingly different: beneath CH and SH core seismic velocities remain higher than their surroundings, but beneath SHV we observe a LVV. Calculation of the seismic velocity anomaly with respect to the structure of the older volcanic centers (Figure 10a) shows that the LVV is 6 to 8 km wide and at least 4 km high, with a volume of over 100 km^3. The maximum seismic velocity reduction is of 0.7 km/s or 12% with respect to CH. The top is at about 3 km depth but the base is not resolved since our resolution analysis shows that objects of the size of the LVV can be resolved at depths of up to 7.5 km but not greater. The volume of the LVV shallower than 7.5 km, with seismic velocity reduced by more than 0.5 km/s, is about 20 km^3. The seismic velocity model would commonly be tested with gravity data but in this case the absence of a gravity base station on Montserrat prevents the integration of onshore and offshore data sets that would be critical to such an analysis.

4.2. Inverse Temperature and Melt Fraction Estimate

[16] The LVV may be caused by variations in lithology, by elevated temperatures and/or by the

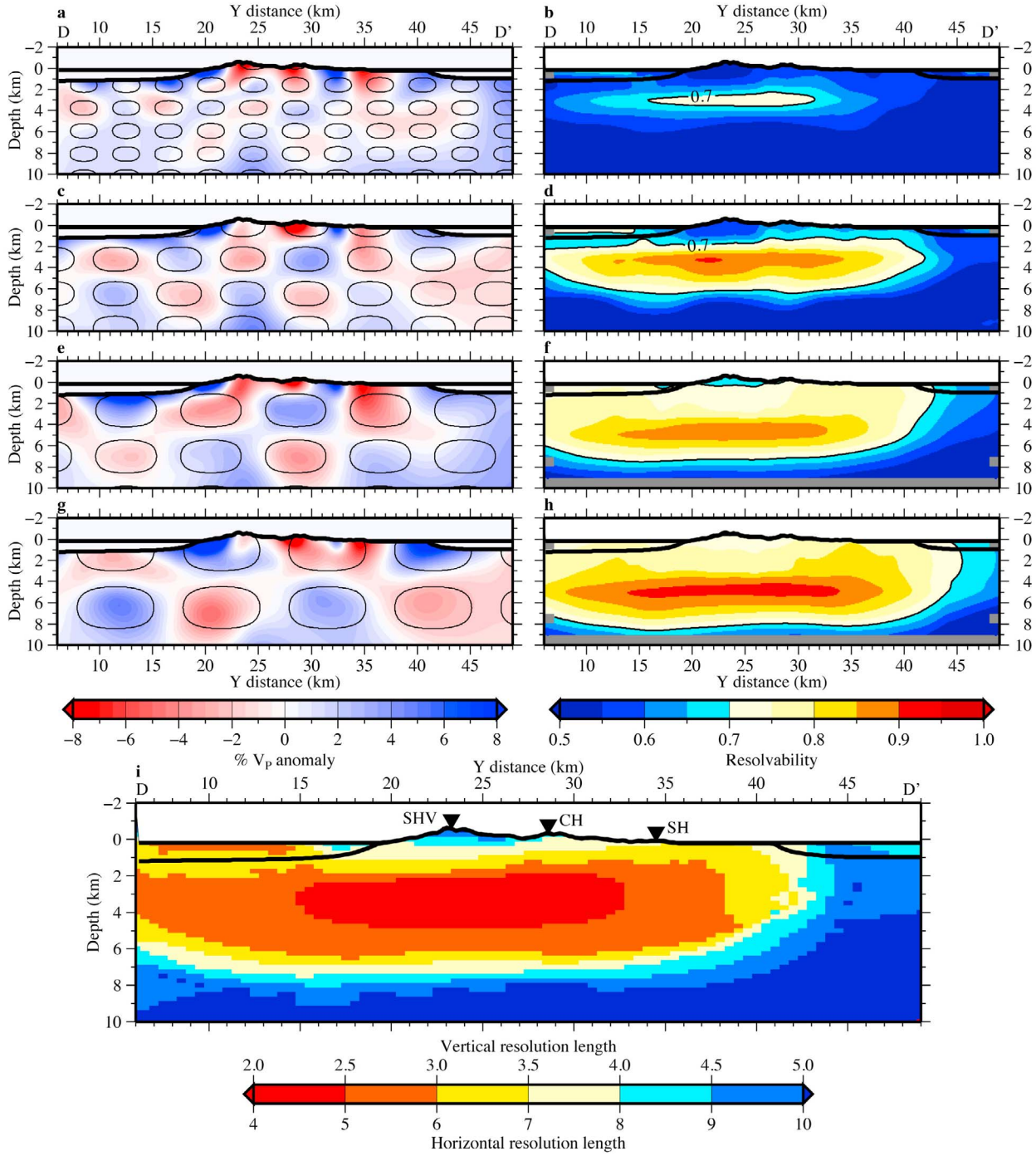

Figure 8. Resolution analysis. Figures 8a–8h are examples of (left) checkerboard tests and (right) mean semblance panels. (a, b) Pattern A: 4 × 4 × 2 km cell size in the *x*, *y* and *z* directions respectively. (c, d) Pattern B: 6 × 6 × 3 km cell size. (e, f) Pattern C: 8 × 8 × 4 km cell size. (g, h) Pattern D: 10 × 10 × 5 km cell size. The 2% contours of the initial perturbation are overlain on the recovered perturbation for reference. (i) Resolution length calculated from interpolation of mean resolvabilities.

presence of partial melt. Significant variations of lithology are unlikely as the three volcanoes have similar compositions [*Harford et al.*, 2002]. To separate the relative contributions of temperature and melt we first assumed that no melt was present and estimated the temperature anomaly expected from the seismic velocity anomaly. We used an expression for the dependence of seismic velocity

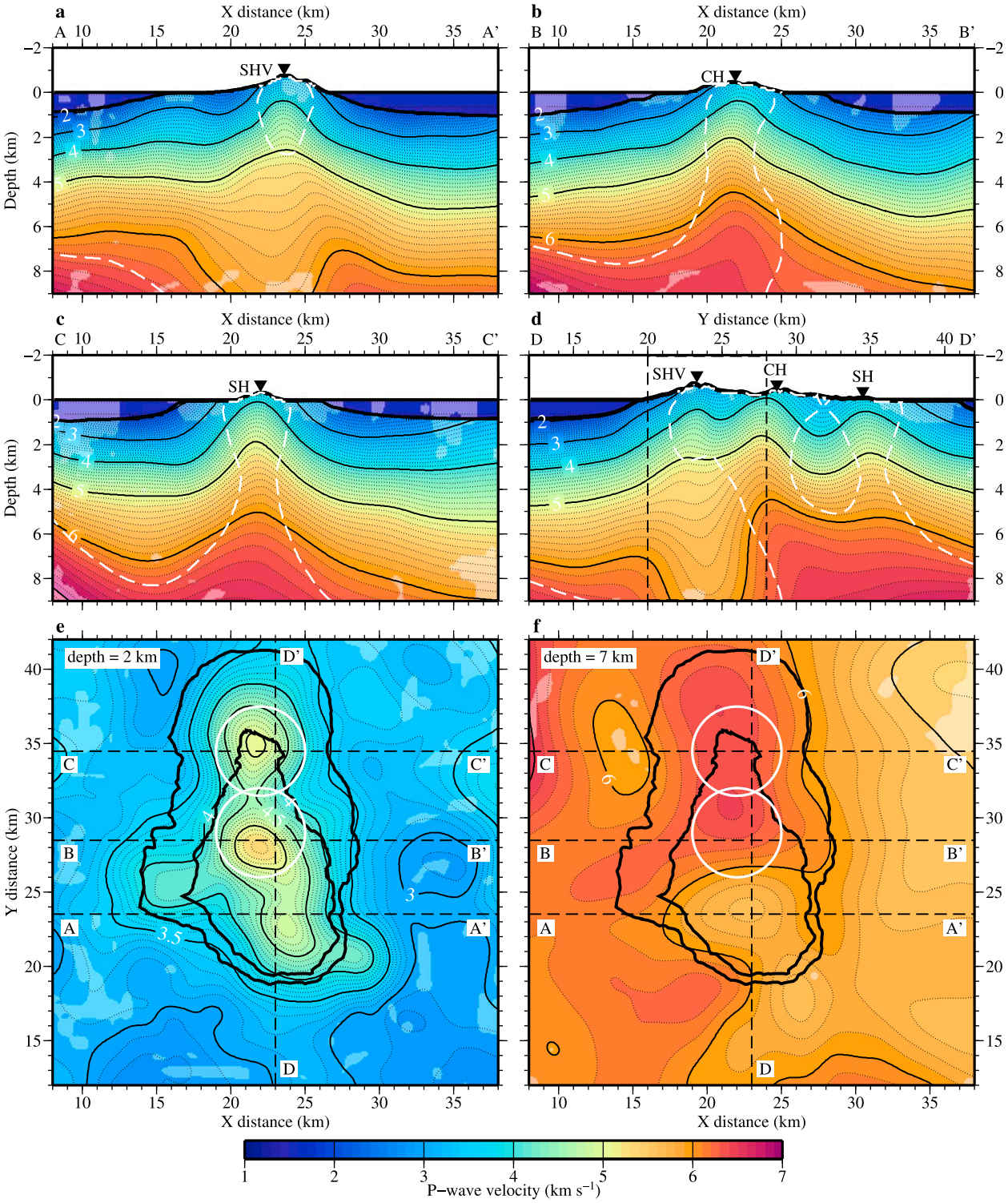

Figure 9. Final seismic velocity model. (a–c) W-E sections through the three major volcanic centers. The high-seismic-velocity cores of the volcanoes are marked with white dashed lines representing 0.25 km/s seismic velocity anomaly contour with respect to the average seismic velocity of the island. (d) S-N section. Dashed frame marks the section of model shown in Figures 10–12. (e, f) Horizontal sections at 2 and 7 km depth below sea level respectively. The coastline and the 200 m depth contour are marked with thick black lines. The white circles bound the area over which the reference model for seismic velocity anomalies was calculated (Figure 10a). Lighter areas have no ray coverage.

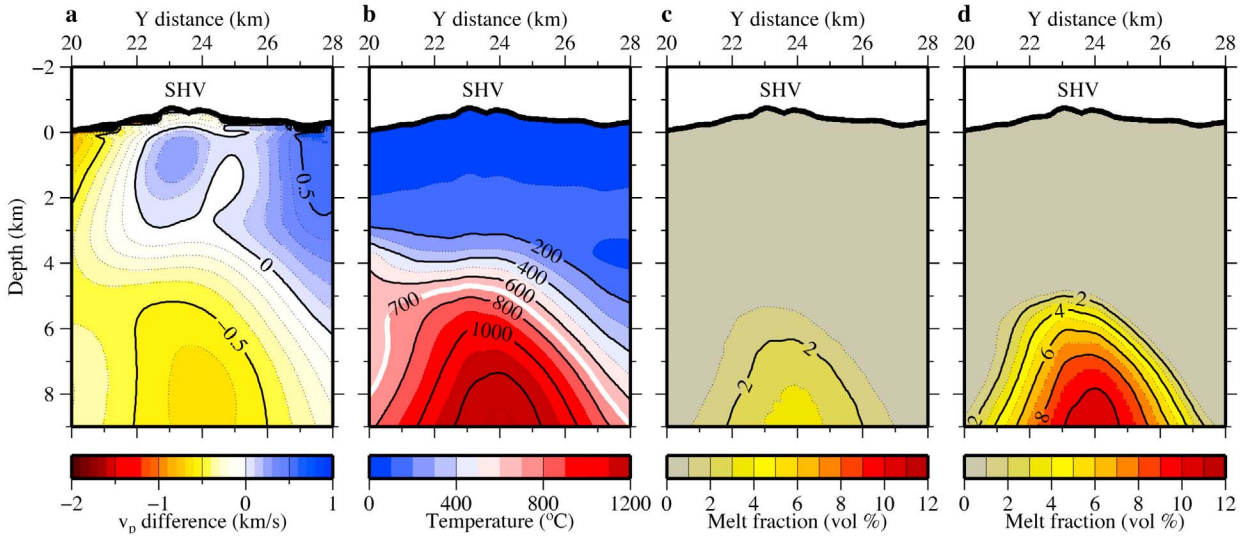

Figure 10. Inverse estimates of temperature and melt fraction. (a) Seismic velocity anomaly along the S-N section DD′ of Figure 9. (b) Temperature model estimated from the seismic velocity anomaly. The background geothermal gradient is 50°C/km. The white contour at 700°C marks the solidus of andesite. (c) Maximum melt fraction calculated from the part of seismic velocity anomaly within the 700°C isotherm that is not accounted for by the rise in temperature, using the thermal model shown in Figure 10b. The melt fraction is calculated assuming the melt resides in interconnected flat pockets (modeled as oblate spheroids, aspect ratio = 0.05). (d) As Figure 10c, but assuming the melt resides in isolated spherical pockets (aspect ratio = 1).

v_P on temperature T that includes the effects of anelasticity and anharmonicity [*Karato*, 1993]:

$$\frac{\partial \ln v_P}{\partial T} = \frac{\partial \ln v_P}{\partial T}\bigg|_{anharmonic} - F(\kappa)\frac{Q^{-1}(f,T)}{\pi}\frac{H^*}{RT^2} \quad (2)$$

where R is the gas constant, H^* is the activation enthalpy for seismic attenuation, and $F(\kappa)$ is a factor that depends on the exponential dependence of Q on frequency. The anharmonic term was assumed to have a constant value of $-8.1 \times 10^{-5}K^{-1}$ [*Christensen*, 1979] and the anelastic term was calculated assuming no frequency dependence ($F = 1$), a relatively low quality factor, $Q = 200$ [*Paulatto et al.*, 2010b], and activation enthalpy H^* of 276 kJ/mol [*Carlstan*, 1982]. We assumed a geothermal gradient of 50°C/km.

[17] Maximum calculated temperatures exceed the solidus of andesite (~700°C) (Figure 10b), indicating the presence of partial melt. Next, estimated temperatures were clipped at the solidus of andesite (assumed to be 700°C) and the part of the velocity anomaly, within the 700°C isotherm, not accounted for by the raised temperatures, was used to estimate melt fraction. In this calculation the temperatures are assumed to be constant at 700°C, since seismic velocities are much more sensitive to the presence of melt than temperature variations. The effect of melt on seismic velocity depends on the geometry and connectivity of the melt pockets and carries a large uncertainty [*Berryman*, 1980; *Dunn et al.*, 2000]. We used different melt pocket geometries to estimate maximum and minimum values of melt fraction, using a self-consistent approach for multiphase composites [*Berryman*, 1980].

[18] The elastic moduli of the composite K^* and μ^* were calculated by solving a pair of coupled equations by numerical iteration:

$$\begin{aligned}\sum_{i=1}^{N} c_i\left(K_i - K^*\right)P^{*i} &= 0\\ \sum_{i=1}^{N} c_i(\mu_i - \mu^*)Q^{*i} &= 0\end{aligned} \quad (3)$$

where c_i are the volume fractions of the constituents and P_i^* and Q_i^* are geometric coefficients that depend on the shape of the grains or melt pockets [*Berryman*, 1980]. The sums are calculated over the constituents that make up the composite. The approach is termed self-consistent because the effect of each grain (or melt pocket) is considered as if it was embedded in a homogeneous material with elastic properties of the composite to be determined. Since the constituents are treated equally and none acts as a matrix the two phases are interchangeable and the approach is valid even for high melt contents.

We considered a medium composed of two phases: solid spherical grains with elastic moduli calculated from the seismic velocities from the tomographic model after the temperature correction, and spheroidal pockets filled with silicic melt with density of 2.3 kg m^{-3} and P-wave velocity of 2.343 km s^{-1} [*Rivers and Carmichael*, 1987], giving a bulk modulus K = 12.7 MPa and shear modulus G = 0 MPa.

[19] We estimated a melt fraction of 3% if the melt pockets are interconnected thin lenses (Figure 10c) and 10% if the pockets are spherical and not interconnected (Figure 10d) [*Dunn et al.*, 2000]. Possible melt fraction values range between 1–15%, when uncertainties in attenuation coefficient Q, geotherm, and other parameters are considered. The two most significant factors are the melt geometry and the attenuation coefficient. A significantly lower Q would mean that more of the anomaly could be explained by variations in temperature alone and would yield a lower melt estimate. In any case these estimates are considerably lower than petrological observations that indicate ~35% melt. However, limited resolution in seismic tomography often leads to underestimated magnitude of LVVs [*Hammond and Humphreys*, 2000], and in turn underestimated melt fraction. In our study the LVV is likely to be considerably smoothed since its dimensions are comparable to the seismic resolution length.

5. Numerical Models of Magma Chamber Growth

[20] To understand the effect of smoothing introduced by seismic tomography and to test compatibility of our model with previous geological and geodetic constraints on the magma chamber properties, we integrated our tomographic results with numerical models of magma chamber growth. We modeled the three-dimensional temperature and melt distribution in the upper crust from incremental growth of a magma chamber by repeated injection of sills at specified depths [*Annen et al.*, 2008]. This model of magma emplacement is supported by observations of intrusive bodies elsewhere [*Searle et al.*, 2003; *de Saint-Blanquat et al.*, 2006; *Michel et al.*, 2008] and by seismic imaging of horizontal reflectors beneath Montserrat that are interpreted as sills [*Byerly et al.*, 2010].

[21] Magma-chamber models were generated by simulating the accumulation and evolution of melt by intrusion of disc-shaped andesite sills in the crust [*Annen et al.*, 2008]. The models are three-dimensional but have a cylindrical symmetry centered on a vertical axis running through the summit of SHV. The cylindrical symmetry allows the three-dimensional volume to be modeled approximately with a two-dimensional grid of square cells. Heat transfer is calculated with an explicit finite difference algorithm [*Tannehill et al.*, 1997]. The boundary conditions are a constant temperature of 0°C at the surface, a symmetry condition on the left boundary and constant temperatures corresponding to the geothermal gradient of 50°C/km on the right boundary. For the bottom boundary we calculate the heat flux due to the presence of a spherical magma reservoir 6 km in radius with a top at a depth of 12.5 km to simulate the presence of a deeper mid-crustal magma reservoir, as proposed by geodetic models based on ground deformation at Montserrat [*Elsworth et al.*, 2008]. Beyond the horizontal extent of this reservoir, the boundary condition is a fixed temperature as determined by the geothermal gradient. To simulate the emplacement of a sill, the cells corresponding to the location and dimensions of the sill and the cells corresponding to a central conduit extending between the lower boundary of the domain and the depth of the sill are set to a temperature of 850°C and to a melt fraction of 35%, which are the estimated characteristics of SHV magma from petrology [*Murphy et al.*, 2000]. The cells beneath the intruded sill are shifted downward to accommodate the new intrusion (Figure 11). This mechanism of floor depression is based on the assumption of mass exchange between a deeper reservoir and the shallow magma chamber we are modeling and is observed in plutons [*Cruden*, 1998]. There is evidence that emplacement depth is determined by crustal rigidity contrasts and stress orientation as well as by density contrast [*Menand*, 2011]. The release of latent heat during crystallization of the magma is modeled with a linear melt/temperature relationship between the solidus at 700°C and a melt fraction of 35% at 850°C. We used the same physical parameters for magma and country rock. Latent heat is 3.5×10^5 J/kg, thermal conductivity is temperature dependent and is derived from diffusivity using equations (1) and (2) of *Whittington et al.* [2009], specific heat is 1000 J/kg°C and density is 2500 kg m^{-3}.

[22] We ran thermal simulations on different timescales (2–60 ka) and for different sill dimensions (r = 1 − 2 km) and emplacement geometries, to predict temperature and melt distribution in the crust. Two models that reflect best understanding of the recent volcanic history and productivity are shown in Figure 12. The temperature and melt

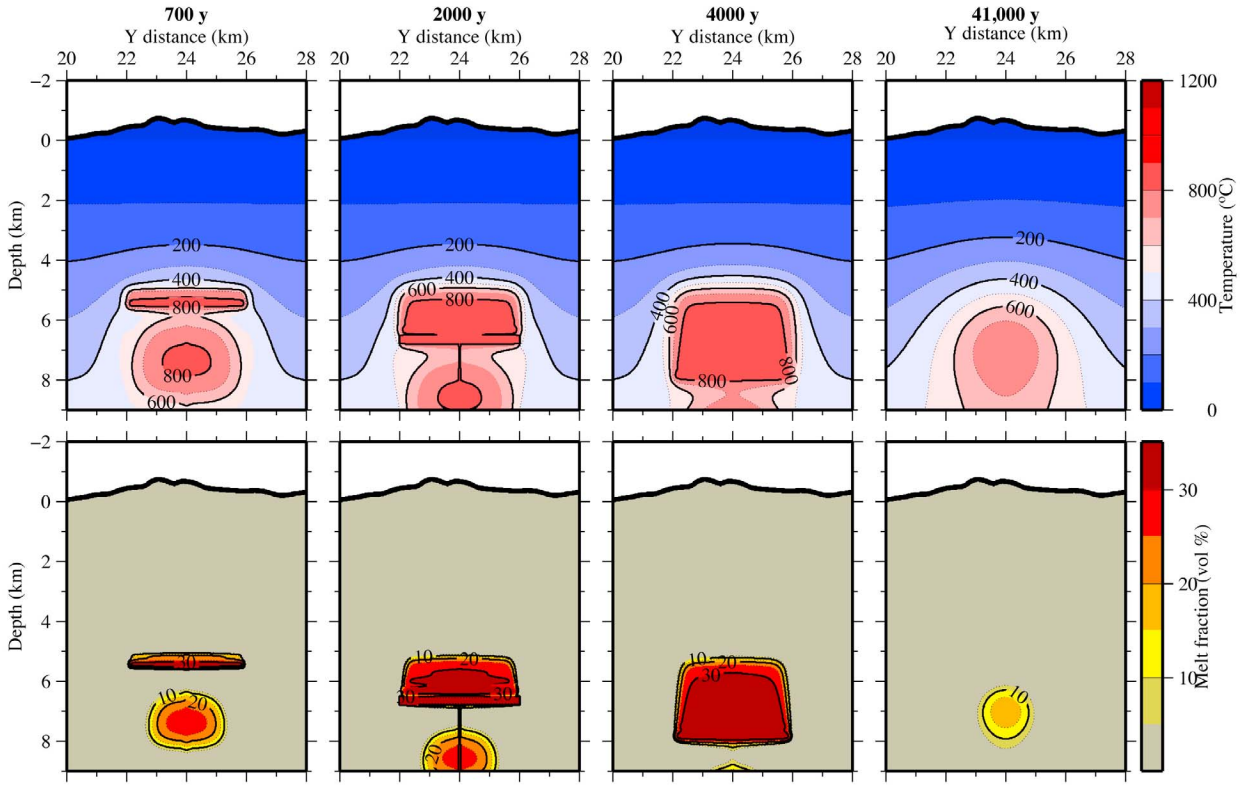

Figure 11. Models of magma chamber growth. Snapshots of magma chamber model A (Figure 12) at different times during and after magma chamber growth. Times are from start of new intrusion event. 700 years: the crust is still heated up by the previous intrusion event but most of the magma chamber has solidified. A new magma chamber is starting to grow at 5.5 km depth. 2000 years: the sills are coalescing and the magma chamber is much thicker. 4000 years: the influx of magma is halted and the magma chamber is at its largest extent. 41,000 years (37,000 years after end of intrusion event): the magma chamber has almost completely solidified, but a thermal anomaly remains.

distributions predicted by these models were used to estimate seismic velocity anomalies using the same methods employed in the inverse estimation of temperature and melt. First, a correction to a background seismic velocity model was calculated by considering the effect of elevated temperatures with the method of *Karato* [1993]. Temperatures were clipped at the solidus of andesite (700°C) since above this temperature the effect of melt would have a much larger effect. Second, the effect of melt distribution was considered with the self-consistent approach of *Berryman* [1980]. The shape of the melt pockets was assumed to be dependent on the melt fraction. Simple models of melt pocket growth, supported by laboratory experiments and field observations suggest that melt develops in thin tubular pockets along crystal edges [*Smith*, 1964; *Waff and Bulau*, 1979; *Mavko*, 1980]. As the melt fraction increases the tubes become thicker. To model this behavior we used spheroidal pockets with aspect ratio equal to half the square root of the reciprocal of the melt fraction (prolate spheroids: aspect ratio <1; oblate spheroids: aspect ratio >1). Melt pockets were assumed to be interconnected (low-frequency approximation). This model gives similar results to the simpler assumption of spherical melt pockets (Figure 13).

[23] The resulting anomalies have much sharper edges and a larger magnitude than the observed seismic velocity anomaly (Figure 12c and 12g). Several factors contribute to the smoothing in seismic tomography: the finite source bandwidth and spatial sampling, picking uncertainties, numerical and theoretical approximations and regularization during inversion [*Nolet*, 1991; *Hansen et al.*, 1999; *Tarantola*, 1987]. At the depth of the LVV, the main cause of smoothing is the limited bandwidth of the seismic signal. We estimated this effect by smoothing the synthetic magma chamber models with a depth-dependent three-dimensional Gaussian filter with width equal to the estimated Fresnel radius for a signal with dominant frequency of 6–25 Hz (see Appendix A for more details on the smoothing filter).

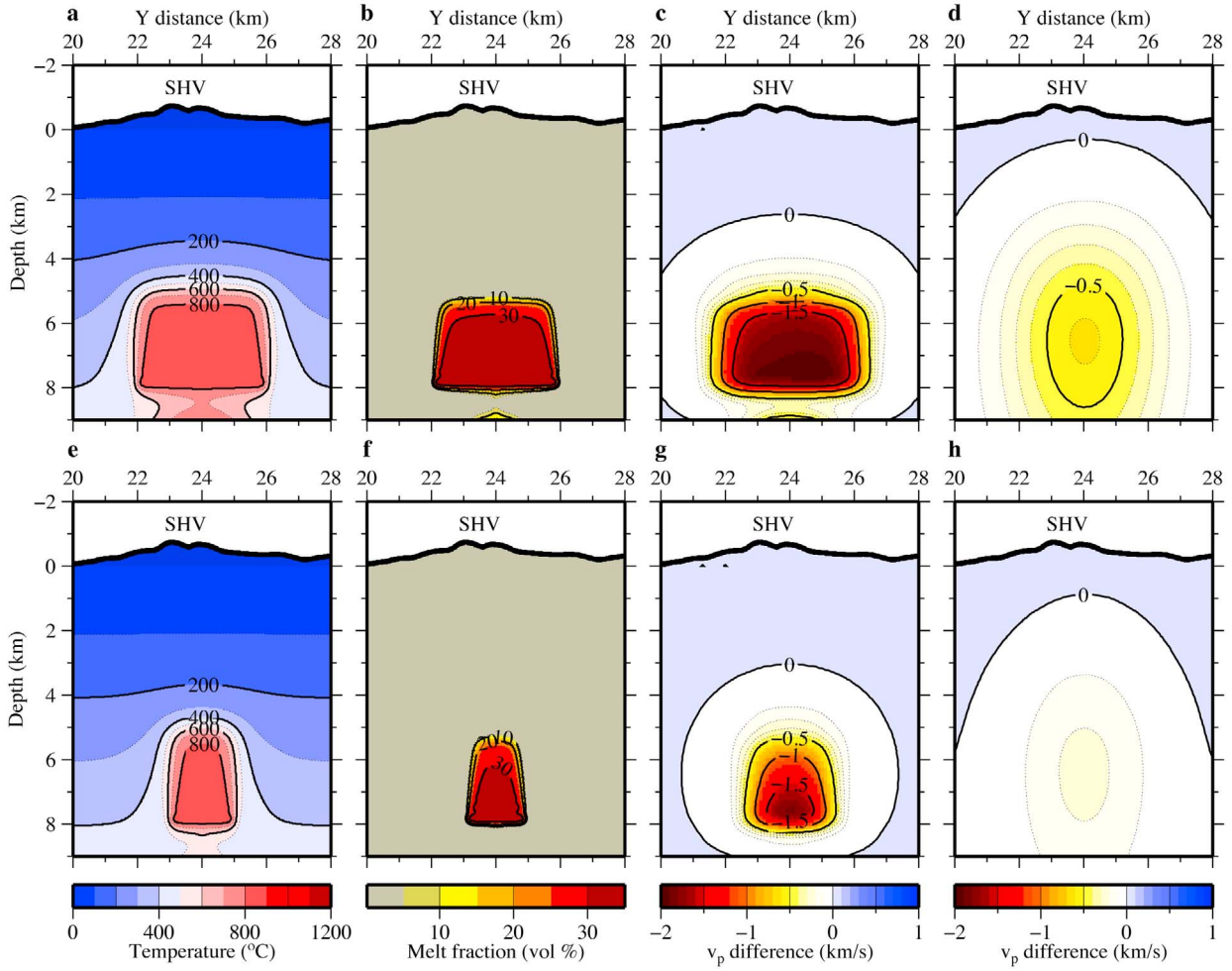

Figure 12. Models of magma chamber accretion and predicted seismic velocity anomaly. Figure 12a–12d: Model A: two successive events of under-accretion of 300-m-thick sills with 2 km radius at 400-year intervals, each starting at 5 km depth and lasting 4000 years, with a 15,000-year repose period. (a) Present-day temperature distribution, corresponding to 4000 years after start of second intrusion event (Figure 11, third panel from left). (b) Melt fraction. (c) P-wave velocity anomaly. (d) P-wave velocity anomaly of filtered model. (e–h) Model B: same as Figures 12a–12d for sills with 1 km radius.

The filter output estimates the sharpest model that can be recovered with travel-time tomography (Figures 12d and 12h).

[24] The filtered synthetic magma chamber models show that only 10–30% of the actual anomaly amplitude is recovered by seismic tomography. The observed LVV is consistent with a magma chamber with size and geometry similar to model A (Figures 12a–12d), which has a volume (with melt fraction greater than 30%) of approximately 13 km^3 between 5.5 km and 7.5 km depth and a maximum melt fraction just below 35%. The total intruded volume is about twice this amount. These estimates are subject to large uncertainties. One of the most significant is the choice of partial melt geometry. Other factors include the timescale of magma chamber accretion, the efficiency of heat transfer (values of thermal diffusivity, possible occurrence of magma convection or hydrothermal circulation), the choice of parameters in the relationship between seismic velocity and temperature, and the design of the smoothing filter. A larger magma chamber ($\sim$20 km^3) could be accommodated if it extended deeper than 7.5 km. Alternatively the magma chamber could be smaller (with volume of $\sim$5 km^3 above 7.5 km depth) if melt was distributed in thin films along crystal faces, since in this case a smaller melt fraction is needed for any given seismic velocity anomaly (Figure 13). The results of model B (Figures 12e–12h) show that a magma chamber with radius smaller than 1 km yields too small a

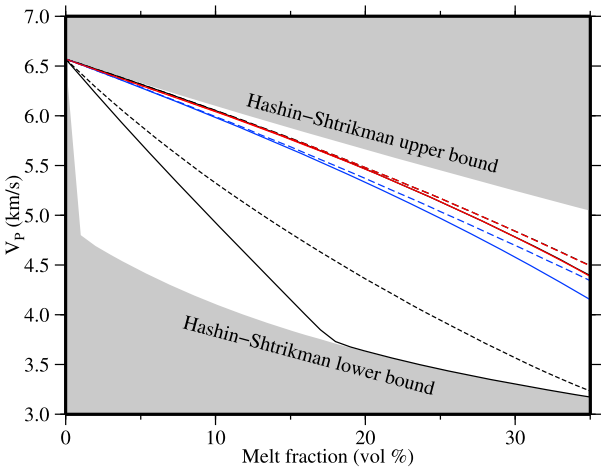

Figure 13. Melt/velocity relationship for different melt pocket geometries. Solid lines: interconnected melt pockets (low-frequency approximation). Dashed lines: isolated melt pockets (high-frequency approximation). Thin black curves: oblate spheroidal pockets (aspect ratio = 0.05); thick black curves (hidden by red curves): spherical pockets (aspect ratio = 1); blue curves: prolate spheroidal pockets (aspect ratio = 10); red curves: spheroidal pockets with variable aspect ratio. The variable-aspect ratio model gives similar results to the model with spherical melt pockets.

seismic velocity anomaly to fit the tomographic results. We conclude that the magma chamber has a radius of 1–2 km and extends from ~5.5 to at least 7.5 km depth.

6. Discussion and Conclusions

[25] Integration of seismic tomography with the numerical models allows us to go beyond simple static constraints on present-day melt distribution. In our models the magma chamber formed by repeated intrusion of andesite sills over a few thousand years, however different emplacement histories can produce similar melt and temperature distributions. A single longer series of sill injections with a slower accretion rate would give a similar present-day seismic anomaly as two shorter series with a faster accretion rate separated by a repose period. Magma chamber growth over several tens of thousand years or more induces thermal anomalies that are too cool and too broad to fit the tomography data. Over-accretion and under-accretion give similar results, but the latter is more consistent with field observations of exhumed granitic plutons [*Wiebe and Collins*, 1998]. In fast-growing magma chambers the emplacement dynamics are likely to be more complex, so under-accretion represents a simplified model. In our preferred model the magma chamber would become almost completely solidified 37,000 years after the last emplacement (Figure 11). Shallow magma chambers of similar volume to our model can become solid over a few thousand to a few tens of thousand years if they are not continuously replenished by new influx [*Annen et al.*, 2008]. This result reinforces the hypothesis that typical arc-volcano magma chambers are transient features, which only exist during active phases.

[26] Our experiment highlights that even a 13 km^3 shallow magma chamber is difficult to detect and constrain with seismic tomography and that associated low-seismic-velocity anomalies may be significantly underestimated. Deeper or smaller magma chambers may be impossible to detect with travel-time seismic tomography. Where an LVV is detected, melt content is poorly constrained by the seismic data, so interpretation must rely on independent constraints. Melt fraction estimated from the velocity anomaly is only 3–10%, similar to estimates at other magmatic systems [*Menke et al.*, 2002; *Haslinger et al.*, 2001]. However, with the use of thermal models and by taking into consideration the smoothing imposed by limited seismic resolution we show that the observed LVV is consistent with the presence of a magma chamber with more than 30% melt as indicated by the observed petrology. Our approach, based on integrating seismic tomography with numerical models of magma chamber formation, incorporating petrological and geodetic constraints, can reveal the characteristics and dynamics of magmatic systems with a level of detail that none of these methods alone has yet achieved.

Appendix A: Fresnel Filter

[27] The finite frequency of the illuminating seismic source means that the travel-time of a seismic wave along a ray depends not only on the seismic velocity of the medium along the ray, but also within a volume surrounding the ray that depends on the frequency content of the signal. This volume is called the Fresnel volume [*Nolet*, 1991] and its radius can be calculated analytically for simple cases [*Williamson*, 1991]. In the upper part of our model the smoothing is dominated by limitations in spatial sampling and the regularization required to compensate for these limitations, but at the depth of the magma chamber, the finite frequency effect becomes dominant. We filtered the synthetic magma chamber models by convolution with a depth-varying smoothing filter designed as a discrete

three-dimensional Gaussian function with full width at half maximum equal to the Fresnel radius of the seismic signal.

[28] For refracted rays, if the seismic signal is monochromatic and the seismic velocity is constant along the ray, the Fresnel radius can be calculated as [*Williamson*, 1991]

$$R = \frac{\pi}{\sqrt{\frac{1}{L}\left(\frac{4\pi}{\lambda} - \frac{1}{L}\right)}} \quad \text{(A1)}$$

where L is the length of the ray and λ is the wavelength of the signal. To express the Fresnel radius as a function of depth we estimated the average length $L(z)$ of refracted rays turning at depth z and the minimum wavelength $\lambda_{min}(z)$ that can be resolved in the signals turning at such depth. $L(z)$ was estimated by linear regression of data from ray tracing in our final model, giving $L(z) = 4.59 \cdot z$. $\lambda_{min}(z)$ was calculated from the average vertical velocity $v(z)$ and the maximum frequency of the signals $f_{max}(z)$. We assumed that the pick uncertainties are equal to half the period corresponding to the dominant frequency of the signal. If the signal is a Ricker wavelet the maximum frequency is approximately double the dominant frequency therefore the reciprocal of the picking error is a good approximation of the maximum frequency of the signal. The resulting filter width varies between 0.5 km at 1 km depth and 4 km at 10 km depth.

Acknowledgments

[29] The SEA-CALIPSO experiment was supported by the National Science Foundation, the National Environment Research Council, the British Geological Survey (BGS), Discovery Channel TV and the British Foreign and Commonwealth Office. MP and EK were partly funded by BGS and RSJS and CA by a European Research Council Advanced Grant (project VOLDIES). We thank Eylon Shalev, Peter Malin, Christine Peirce, James Hammond, Kate Kenedi, Glen Mattioli, Larry Brown, Brian Baptie and the many people who contributed to the field campaign. We thank two anonymous reviewers for their insightful comments.

References

Alfaro, R., B. Brandsdóttir, D. P. Rowlands, R. S. White, and M. T. Gudmundsson (2007), Structure of the Grímsvötn central volcano under the Vatnajökull icecap, Iceland, *Geophys. J. Int.*, *168*, 863–876, doi:10.1111/j.1365-246X.2006.03238.x.

Annen, C., M. Pichavant, O. Bachmann, and A. Burgisser (2008), Conditions for the growth of a long-lived shallow crustal magma chamber below Mount Pelee volcano (Martinique, Lesser Antilles Arc), *J. Geophys. Res.*, *113*, B07209, doi:10.1029/2007JB005049.

Aspinall, W. P., A. D. Miller, L. L. Lynch, J. L. Latchman, R. C. Stewart, R. A. White, and J. A. Power (1998), Soufriére Hills eruption, Montserrat, 1995–1997: volcanic earthquake locations and fault plane solutions, *Geophys. Res. Lett.*, *25*(18), 3397–3400.

Berryman, J. G. (1980), Long wavelength propagation in composite elastic media I. Spherical inclusions and II. Ellipsoidal inclusions, *J. Acoust. Soc. Am.*, *68*, 1809–1831.

Brandsdottir, B., W. Menke, P. Einarsson, R. S. White, and R. K. Staples (1997), Faroe-Iceland Ridge Experiment: 2. Crustal structure of the Krafla central volcano, *J. Geophys. Res.*, *102*(B4), 7867–7886.

Byerly, K., L. Brown, B. Voight, and V. Miller (2010), Reflection imaging of deep structure beneath Montserrat using microearthquake sources, *Geophys. Res. Lett.*, *37*, L00E20, doi:10.1029/2009GL041995.

Carlstan, Y. (1982), The transition from high temperature creep to fracture in Maryland diabase, *J. Geophys. Res.*, *87*, 6781–6790.

Christensen, N. I. (1979), Compressional wave velocities in rocks at high temperatures and pressures, critical thermal gradients, and crustal low-velocity zones, *J. Geophys. Res*, *86*, 6849–6857.

Christeson, G. L., P. Mann, A. Escalona, and T. J. Aitken (2008), Crustal structure of the Caribbean–northeastern South America arc-continent collision zone, *J. Geophys. Res.*, *113*, B08104, doi:10.1029/2007JB005373.

Coffin, M. F., L. M. Gahagan, and L. A. Lawver (1998), Present-day plate boundary digital data compilation, *Tech. Rep. 174*, Univ. of Tex., Austin.

Cruden, A. R. (1998), On the emplacement of tabular granites, *J. Geol. Soc.*, *155*, 853–862.

de Saint-Blanquat, M., et al. (2006), Mechanisms and duration of non-tectonically assisted magma emplacement in the upper crust: The Black Mesa pluton, Henry Mountains, Utah, *Tectonphysics*, *428*(1), 1–31.

Dunn, R. A., D. R. Toomey, and S. C. Solomon (2000), Three-dimensional seismic structure and physical properties of the crust and shallow mantle beneath the East Pacific Rise at 9°30′N, *J. Geophys. Res.*, *105*(B10), 23,357–23,555.

Elsworth, D., G. Mattioli, J. Taron, B. Voight, and R. Herd (2008), Implications of magma transfer between multiple reservoirs on eruption cycling, *Science*, *322*, 246–248.

Evangelidis, C. P., T. A. Minshull, and T. J. Henstock (2004), Three-dimensional crustal structure of Ascension Island from active source seismic tomography, *Geophys. J. Int.*, *159*(1), 311–325, doi:10.1111/j.1365-246X.2004.02396.x.

Foroozan, R., D. Elsworth, B. Voight, and G. S. Mattioli (2010), Dual reservoir structure at Soufriére Hills Volcano inferred from continuous GPS observations and heterogeneous elastic modeling, *Geophys. Res. Lett.*, *37*, L00E12, doi:10.1029/2010GL042511.

Hammond, C., and E. D. Humphreys (2000), Upper mantle seismic wave velocity: Effects of realistic partial melt geometries, *J. Geophys. Res.*, *105*(B5), 10,975–10,986.

Hansen, T. M., S. C. Singh, and B. H. Jacobsen (1999), Sensitivity of seismic wide-angle wave-field and first arrival times to fine scale crustal structure and Moho topography, *Geophys. Res. Lett.*, *26*(16), 2573–2576.

Harford, C. L., M. S. Pringle, R. S. J. Sparks, and S. R. Young (2002), The Volcanic evolution of Montserrat using $^{40}Ar/^{39}Ar$ geochronology, in *The Eruption of Soufriére Hills Volcano, Montserrat, From 1995 to 1999*, edited by T. H. Druitt and B. P. Kokeelar, *Geol. Soc. Mem.*, *21*, 93–113.

Haslinger, F., C. Thurber, M. Mandernach, and P. Okubo (2001), Tomographic image of P-velocity structure beneath Kilauea's East Rift Zone and South Flank: Seismic evidence for a deep magma body, *Geophys. Res. Lett.*, *28*(2), 375–378.

Hobro, J. W. D., S. C. Singh, and T. A. Minshull (2003), Three-dimensional tomographic inversion of combined reflection and refraction seismic traveltime data, *Geophys. J. Int.*, *152*, 79–93.

Karato, S. (1993), Importance of anelasticity in the interpretation of seismic tomography, *Geophys. Res. Lett.*, *20*(5), 1623–1626.

Kenedi, C. L., R. S. J. Sparks, P. Malin, B. Voight, S. Dean, T. Minshull, M. Paulatto, C. Peirce, and E. Shalev (2010), Contrasts in morphology and deformation offshore Montserrat: New insights from the SEA-CALIPSO marine cruise data, *Geophys. Res. Lett.*, *37*, L00E25, doi:10.1029/2010GL043925.

Lees, J. M. (2007), Seismic tomography of magmatic systems, *J. Volcanol. Geotherm. Res.*, *167*(1–4), 37–56, doi:10.1016/j.jvolgeores.2007.06.008.

Le Friant, A., C. Harford, C. Deplus, G. Boudon, R. S. J. Sparks, R. A. Herd, and J. C. Komorowski (2004), Geomorphological evolution of Montserrat (West Indies): Importance of flank collapse and erosional processes, *J. Geol. Soc.*, *161*, 147–160.

Mattioli, G. S., R. A. Herd, M. H. Strutt, G. Ryan, C. Widiwijayanti, and B. Voight (2010), Long term surface deformation of Soufriére Hills Volcano, Montserrat from GPS geodesy: Inferences from simple elastic inverse models, *Geophys. Res. Lett.*, *37*, L00E13, doi:10.1029/2009GL042268.

Mavko, G. (1980), Velocity and attenuation in partially molten rocks, *J. Geophys. Res.*, *85*(B10), 5173–5189.

Menand, T. (2011), Physical controls and depth of emplacement of igneous bodies: A review, *Tectonphysics*, *500*(1–4), 11–19.

Menke, W., M. West, and M. Tolstoy (2002), Shallow-crustal magma chamber beneath the axial high of the Coaxial segment of Juan de Fuca Ridge at the source site of the 1993 eruption, *Geology*, *30*(4), 359–362.

Michel, J., J. Baumgartner, B. Putlitz, U. Schaltegger, and M. Ovtcharova (2008), Incremental growth of the Patagonian Torres del Paine laccolith over 90 k.y, *Geology*, *36*, 459–462.

Minshull, T. A., C. Peirce, and M. C. Sinha (2005), Multidisciplinary, sub-seabed geophysical imaging, *Sea Technol.*, *46*(10), 27–31.

Murphy, M. D., R. S. J. Sparks, J. Barclay, M. R. Carroll, and T. S. Brewer (2000), Remobilization of andesite magma by Intrusion of mafic magma at the Soufriére Hills Volcano, Montserrat, West Indies, *J. Petrol.*, *41*(1), 21–42.

Nolet, G. (1991), Imaging the deep Earth: Technical possibilities and theoretical limitations, in *Proc. XXIIth Assembly ESC Barcelona 1990*, edited by A. Rocca and D. Mayer-Rosa, pp. 107–115, Servei Geol. de Catalunya, Barcelona, Spain.

Paulatto, M., et al. (2010a), Upper crustal structure of an active volcano with refraction/reflection tomography, Montserrat, Lesser Antilles, *Geophys. J. Int.*, *180*(2), 685–696.

Paulatto, M., T. A. Minshull, and T. J. Henstock (2010b), Constraints on an intrusive system beneath the Soufriére Hills Volcano, Montserrat, from finite difference modeling of a controlled source seismic experiment, *Geophys. Res. Lett.*, *37*, L00E01, doi:10.1029/2009GL041805.

Rivers, M. L., and I. S. E. Carmichael (1987), Ultrasonic studies of silicate melts, *J. Geophys. Res.*, *82*, 9247–9270.

Searle, M. P., R. L. Simpson, R. D. Law, R. R. Parrish, and D. J. Waters (2003), The structural geometry, metamorphic and magmatic evolution of the Everest massif, High Himalaya of Nepal-South Tibet, *J. Geol. Soc.*, *160*, 345–366.

Seher, T., S. C. Singh, W. C. Crawford, and J. Escartin (2010), Upper crustal velocity structure beneath the central Lucky Strike Segment from seismic refraction measurements, *Geochem. Geophys. Geosyst.*, *11*, Q05001, doi:10.1029/2009GC002894.

Shalev, E., et al. (2010), Three-dimensional seismic velocity tomography of Montserrat from the SEA-CALIPSO offshore/onshore experiment, *Geophys. Res. Lett.*, *37*, L00E17, doi:10.1029/2010GL042498.

Shepherd, J. B., J. F. Tomblin, and D. A. Woo (1971), Volcano-seismic crisis in Montserrat, West Indies, 1966–67, *Bull. Volcanol.*, *35*, 143–163.

Smith, C. S. (1964), Some elementary principles of polycrystalline micro-structure, *Metall. Rev.*, *9*, 1–48.

Tannehill, J. C., D. A. Anderson, and R. H. Pletcher (1997), *Computational Fluid Mechanics and Heat Transfer*, 792 pp., Taylor and Francis, Philadelphia, Penn.

Tarantola, A. (1987), *Inverse Problem Theory*, Elsevier, Amsterdam.

Virieux, J., and V. Farra (1991), Ray tracing in 3-D complex isotropic media: An analysis of the problem, *Geophysics*, *56*, 2057–2069.

Voight, B., et al. (2006), Unprecedented pressure increase in deep magma reservoir triggered by lava dome collapse, *Geophys. Res. Lett.*, *33*, L03312, doi:10.1029/2005GL024870.

Voight, B., C. Widiwijayanti, G. Mattioli, D. G. S. Elsworth, D. Hidayat, and M. H. Strutt (2010a), Magma-sponge hypothesis and stratovolcanoes: Case for a compressible reservoir and quasi-steady deep influx at Soufriére Hills Volcano, Montserrat, *Geophys. Res. Lett.*, *37*, L00E05, doi:10.1029/2009GL041732.

Voight, B., et al. (2010b), Active source seismic experiment peers under Soufriére Hills Volcano, *Eos Trans. AGU*, *91*(28), 245, doi:10.1029/2010EO280002.

Waff, H. S., and J. R. Bulau (1979), Equilibrium fluid distribution in an ultramafic partial melt under hydrostatic stress conditions, *J. Geophys. Res.*, *84*(B11), 6109–6114, doi:10.1029/JB084iB11p06109.

Whittington, A. G., A. M. Hofmeister, and P. I. Nabelek (2009), Temperature-dependent thermal diffusivity of the Earth's crust and implications for magmatism, *Nature*, *458*, 319–321.

Wiebe, R. A., and W. J. Collins (1998), Depositional features and stratigraphic sections in granitic plutons: implications for the emplacement and crystallization of granitic magma chambers, *J. Struct. Geol.*, *20*, 1273–1289.

Williamson, P. R. (1991), A guide to the limits of resolution imposed by scattering in ray tomography, *Geophysics*, *56*(2), 202–207.

Zellmer, G. F., R. S. J. Sparks, C. J. Hawkesworth, and M. Wiedenbeck (2003), Magma emplacement and remobilization timescales beneath Montserrat: Insights from Sr and Ba zonation in Plagioclase, *J. Petrol.*, *44*(8), 1413–1431.

Zelt, A. C. (1998), Lateral velocity resolution from 3-d seismic refraction data, *Geophys. J. Int.*, *135*, 1101–1112.